



## Catalytic methane combustion over Pd/ZrO<sub>2</sub> catalysts: Effects of crystalline structure and textural properties

Eunpyo Hong<sup>a</sup>, Chansong Kim<sup>a</sup>, Dong-Hee Lim<sup>b</sup>, Hyo-Jin Cho<sup>b</sup>, Chae-Ho Shin<sup>a,\*</sup>

<sup>a</sup> Department of Chemical Engineering, Chungbuk National University, Chungbuk 28644, Republic of Korea

<sup>b</sup> Department of Environmental Engineering, Chungbuk National University, Chungbuk 28644, Republic of Korea



### ARTICLE INFO

#### Keywords:

Zirconia  
Pd/ZrO<sub>2</sub> catalyst  
Tetragonal  
Methane combustion  
Density functional theory

### ABSTRACT

Zirconia supports were synthesized via a precipitation method, and the effects of crystalline structure and textural properties of ZrO<sub>2</sub> on the methane combustion reaction were investigated using the Pd/ZrO<sub>2</sub> catalysts. Upon increasing the digestion temperature, the crystalline structure of ZrO<sub>2</sub> was transformed from the mixed phase (monoclinic and tetragonal) to the pure tetragonal phase, and these tetragonal ZrO<sub>2</sub> supported Pd catalysts exhibited good hydrothermal stabilities. In addition, the BET surface areas of the tetragonal ZrO<sub>2</sub> supports could also be tuned by varying the digestion time and calcination temperature, and the catalysts supported on ZrO<sub>2</sub> having lower BET surface areas exhibited enhanced catalytic activities. Therefore, the Pd/ZrO<sub>2</sub>(85) catalyst, which had a tetragonal structure in addition to the smallest BET surface area, gave the optimal catalytic performance. This is likely due to larger PdO particles being formed on this ZrO<sub>2</sub>(85) support, thereby resulting in a highly reducible PdO species. Finally, variations in reducibility between the monoclinic and the tetragonal supported catalysts were clearly calculated by the density functional theory.

### 1. Introduction

Catalytic methane combustion has received growing attention for a number of reasons. Firstly, when compared to conventional thermal combustion, catalytic methane combustion can be operated at relatively low temperatures (i.e., < 500 °C), and so the reaction can be effectively carried out with low emissions of thermal NO<sub>x</sub> and CO [1–3]. Secondly, the removal of methane from gaseous emissions is of particular importance, as methane is the second largest contributor (~19%) to global warming after carbon dioxide (~64%), and exhibits a significantly greater (~21 times) global warming potential than carbon dioxide [4–7]. In addition, methane is the most difficult hydrocarbon to oxidize when compared to ethane, propane, and other long-chain hydrocarbons [8–10]. The methane combustion reaction can therefore be employed as a model reaction to determine the oxidation abilities of catalysts. For the reasons stated above, the catalytic methane combustion reaction has been extensively studied for various industrial applications, such as natural gas-fueled engines, boilers, and exhaust gas control catalysts.

The supported Pd catalysts are known to be amongst some of the most active catalysts for the methane combustion reaction [2,11–13], and various supports such as Al<sub>2</sub>O<sub>3</sub> [2,14–17], CeO<sub>2</sub> [18], SnO<sub>2</sub> [19,20], SiO<sub>2</sub> [21], and ZrO<sub>2</sub> [1,13,22,23] have been widely studied for

decades. However, improving the low temperature activity [5,7,24,25], sulfur poisoning resistance [26–29], and hydrothermal stability [2,6,14,22,30] is still a challenge to resolve. In particular, the hydrothermal stabilities are very important, as the reaction feeds normally contain water vapor, and water is also produced by the combustion reaction itself (i.e., CH<sub>4</sub> + 2O<sub>2</sub> → CO<sub>2</sub> + 2H<sub>2</sub>O). Although Pd/Al<sub>2</sub>O<sub>3</sub> catalysts are relatively active under dry conditions, they undergo severe deactivation in the presence of water vapor due to the formation of inactive Pd(OH)<sub>2</sub> species during the reaction [2,31,32]. In contrast, ZrO<sub>2</sub> supported catalysts have often been shown to exhibit excellent hydrothermal stabilities [22,23].

In our previous work [33], ZrO<sub>2</sub> supports were synthesized under a range of digestion conditions. It should be noted that the synthetic route to hydrous zirconia is closely related to hydrolytic polymerization [34,35], and dissolution and recrystallization occur during the digestion process. Thus, the digestion temperature and time employed during preparation of the ZrO<sub>2</sub> support significantly influence on its resulting characteristics [36–39]. For example, upon increasing the digestion temperature, dissolution and recrystallization are promoted, resulting in small homogeneous particles with increased Brunauer–Emmett–Teller (BET) surface areas. An increase in the digestion time also leads to similar effects. In addition to these variations in the textural properties, the crystalline structure also varied. More specifically,

\* Corresponding author.

E-mail address: [chshin@chungbuk.ac.kr](mailto:chshin@chungbuk.ac.kr) (C.-H. Shin).

as the digestion temperature is increased, the crystalline phase changes from a mixed (monoclinic and tetragonal) to a pure tetragonal phase.

Thus, we herein reported the precipitation of hydrous zirconia using an NH<sub>4</sub>OH solution as the precipitant, followed by digestion of the resulting precursor solution at a range of temperatures. Following preparation of the various supports, the effects of varying the digestion temperature, digestion time, and calcination temperature were examined. Subsequently, the effects of different crystalline phases and textural properties on the methane combustion reaction were investigated in detail. In particular, the main purpose of this work is improving the hydrothermal stability under fuel-lean conditions, and thus the results obtained from isothermal reaction in the presence of water vapor will be carefully discussed.

## 2. Experimental methods

### 2.1. Catalyst preparation

#### 2.1.1. Effects of digestion temperature

The ZrO<sub>2</sub> supports were prepared via a previously reported chemical precipitation method [33]. Initially, the ZrOCl<sub>2</sub>·8H<sub>2</sub>O precursor (98%, Sigma-Aldrich) was dissolved in deionized water at room temperature with vigorous stirring to give a 0.5 M aqueous solution of the precursor (200 mL). A solution of NH<sub>4</sub>OH (28 wt%, SK Chemical) was then added dropwise to the precursor solution to give a pH of 9.5. The resulting solution was further treated for 48 h at the desired temperature (i.e., 30–100 °C), where the reactor was fitted with a reflux condenser to prevent solvent loss and changes in the mother liquor composition (this process is called “digestion”). The precipitate was then filtered and washed with deionized water, and the obtained product was dried at 60 °C overnight prior to calcination at 600 °C for 6 h under a flow of air. To improve reader’s understanding, the experimental parameters for support preparation such as digestion temperature, digestion time, and calcination temperature are summarized in Table 1.

The desired 1 wt% Pd/ZrO<sub>2</sub> catalysts were synthesized via an incipient wetness impregnation method using a 10 wt% solution of Pd (NO<sub>3</sub>)<sub>2</sub> (Heesung Catalysts Corp.). Following the impregnation of Pd, the catalysts were dried at 60 °C for 24 h, then calcined at 600 °C for 2 h. The synthesized supports and catalysts were labeled as ZrO<sub>2</sub>(x) and Pd/ZrO<sub>2</sub>(x), respectively, where x indicates the digestion temperature employed during synthesis of the hydrous zirconia support.

#### 2.1.2. Effects of digestion time and calcination temperature

To investigate the effect of the BET surface area on the catalytic activity, the catalysts were prepared according to the procedure outlined above for the Pd/ZrO<sub>2</sub>(100) catalyst, but with variation in the digestion time and calcination temperature employed during preparation of the support. Three additional samples, namely ZrO<sub>2</sub>(A), ZrO<sub>2</sub>(B), and ZrO<sub>2</sub>(C), were employed, where ZrO<sub>2</sub>(A) and ZrO<sub>2</sub>(B) were aged for 240 h and calcined at 700 and 600 °C, respectively. The ZrO<sub>2</sub>(C) was obtained commercially (monoclinic ZrO<sub>2</sub>, SZ 31164, Saint Gobain

NorPro) and was used without additional calcination. Following the impregnation of 1 wt% Pd on the supports via an incipient wetness method, the samples were calcined at 600 °C for 2 h, and the three resulting catalyst samples were denoted as Pd/ZrO<sub>2</sub>(A), Pd/ZrO<sub>2</sub>(B), and Pd/ZrO<sub>2</sub>(C). The experimental variables for Pd/ZrO<sub>2</sub>(A), Pd/ZrO<sub>2</sub>(B), and Pd/ZrO<sub>2</sub>(C) are summarized in Table 1.

## 2.2. Characterization

To investigate the BET surface areas, total pore volumes, and average pore diameters of the samples, N<sub>2</sub>-sorption isotherms were measured using an ASAP 2020 Surface Area and Porosity Analyzer (Micromeritics). Prior to measurements, the samples were degassed at 250 °C for 5 h under vacuum. High resolution transmission electron microscopy (HR-TEM) images were taken from a JEM 2100F (JEOL). To identify the crystalline structures of the supports and the catalysts, X-ray diffraction (XRD) was conducted on a D8 Discover with GADDS X-ray diffractometer (Bruker AXS) using Cu K $\alpha$  radiation with 40 kV acceleration voltage and 40 mA applied current (scan size = 0.01°/step and scan rate = 0.2 s/step). From the XRD patterns, the crystallite size (D, nm) was calculated using the Scherrer equation (Eq. (1)):

$$D = k\lambda/\beta\cos\theta \quad (1)$$

where k is the shape factor of the particle (0.89),  $\lambda$  is the X-ray wavelength (0.15406 nm),  $\beta$  is the corrected full width at half maximum in radian, and  $\theta$  is the Bragg diffraction angle in degrees. The volume fraction of the tetragonal phase ( $V_T$ ) was estimated using the following empirical formulae (Eqs. (2)–(4)) [33,40–42]:

$$V_M = 1.311X_M/(1 + 0.311X_M) \quad (2)$$

$$X_M = [I_M(1\ 1\ 1) + I_M(\bar{1}\ 1\ 1)]/[I_M(1\ 1\ 1) + I_M(\bar{1}\ 1\ 1) + I_T(0\ 1\ 1)] \quad (3)$$

$$V_T = 1 - V_M \quad (4)$$

where  $V_M$  is the volume fraction of the monoclinic phase, and  $I_M$  and  $I_T$  are the peak intensities of the monoclinic and tetragonal phases, respectively.

The different oxidation states existing in the Pd/ZrO<sub>2</sub> catalysts were identified by X-ray photoelectron spectroscopy (XPS) using an PHI Quantera-II (Ulvac-PHI) photoelectron spectrometer (Al K $\alpha$  radiation;  $h\nu = 1486.6$  eV) with analyzer pass-energy of 55 eV and step size of 0.05 eV (time per step = 20 ms), and the spectra were calibrated using the binding energy of adventitious carbon (C 1s, 284.6 eV) as a standard. To determine the peak areas and positions, the deconvolutions of the Pd 3d<sub>5/2</sub> and Zr 3d<sub>5/2</sub> spectra were carried out using a Gaussian–Lorentzian curve-fitting method after background subtraction by the Shirley method. The reduction characteristics of the supported PdO species were investigated by CH<sub>4</sub> temperature-programmed reduction (CH<sub>4</sub>-TPR). More specifically, the sample (0.1 g) was loaded in a fixed bed quartz reactor and pretreated at 500 °C for 1 h under a flow of air. After this time, the sample was cooled to 100 °C under a flow of air, then heated to 400 °C with a heating rate of 5 °C/min under 0.5% CH<sub>4</sub>/N<sub>2</sub> (total flow rate = 80 cm<sup>3</sup>/min). The quantity of CH<sub>4</sub> consumed was analyzed using an infrared gas analyzer (Model 7500, Teledyne Analytical Instruments). To measure the degree of CO chemisorption on the supported Pd, volumetric CO chemisorption was performed using an ASAP 2020 (Micromeritics). Prior to analysis, the catalyst was reduced under a flow of H<sub>2</sub> for 1 h at 200 °C. The adsorption measurements were performed at 100 °C, and the dispersion and particle size were calculated from the total CO uptake by assuming a stoichiometry of CO/Pd = 1 [6,15,16,21,43].

**Table 1**  
The experimental variables for support preparation.

Sample	Digestion temperature (°C)	Digestion time (h)	Calcination temperature (°C)
ZrO <sub>2</sub> (30)	30	48	600
ZrO <sub>2</sub> (50)	50	48	600
ZrO <sub>2</sub> (70)	70	48	600
ZrO <sub>2</sub> (85)	85	48	600
ZrO <sub>2</sub> (100)	100	48	600
ZrO <sub>2</sub> (A)	100	240	700
ZrO <sub>2</sub> (B)	100	240	600
ZrO <sub>2</sub> (C) <sup>a</sup>	–	–	–

<sup>a</sup> ZrO<sub>2</sub>(C) is a commercial support, and used without further treatment.

### 2.3. Methane combustion reaction

For the methane combustion reaction, the Pd/ZrO<sub>2</sub> catalyst (0.1 g) was loaded into a quartz fixed bed reactor (I.D. 12 mm). Prior to the reaction, pretreatment was carried out at 500 °C under a flow of air for 1 h (50 cm<sup>3</sup>/min). The reaction composition was fixed at 0.1% CH<sub>4</sub>/3.15% O<sub>2</sub>/N<sub>2</sub> balance with a total flow rate of 400 cm<sup>3</sup>/min in either the presence or absence of 10 vol% water vapor for both temperature-programmed reaction (T.P. reaction) and isothermal reaction (GHSV = 240,000 cm<sup>3</sup> g<sup>-1</sup> h<sup>-1</sup>). After the pretreatment, the reactor was cooled to 100 °C for the T.P. reaction, and it was carried out with temperature from 100 to 600 °C at a rate of 5 °C/min. For the cyclic T.P. reactions, the heating and cooling cycles were repeated three times. The isothermal reaction proceeded at 450 and 500 °C after the pretreatment, and the CH<sub>4</sub> concentration was measured using an infrared gas analyzer (Model 7500, Teledyne Analytical Instruments). Finally, the CH<sub>4</sub> conversion (%) was calculated according to Eq. (5):

$$\text{CH}_4 \text{ conversion } (X, \%) = \frac{\text{CH}_4 \text{ in} - \text{CH}_4 \text{ out}}{\text{CH}_4 \text{ in}} \times 100 \quad (5)$$

where CH<sub>4</sub> in and CH<sub>4</sub> out are concentrations of CH<sub>4</sub> at the inlet and outlet, respectively. The reaction schematic including water feeding system and the detail method for calculation of CH<sub>4</sub> conversion are indicated in supplementary information (Fig. S1).

### 2.4. Computational methodology

Spin-polarized density functional theory (DFT) calculations were performed using the Vienna *ab initio* Simulation Package (VASP) [44–47] with the projector-augmented wave (PAW) [48,49] method. Electron exchange-correlation functionals were represented with the generalized gradient approximation (GGA), and the model of Perdew, Burke, and Ernzerhof (PBE) [50] was used for the nonlocal corrections. A kinetic energy cutoff of 400 eV was used with a plane-wave basis set [51].

A rhombus-shaped supercell of 6.91 × 6.69 × 21.5 Å and a rectangular-shaped supercell of 7.26 × 6.39 × 24.0 Å with periodic boundary conditions were used for monoclinic *m*-ZrO<sub>2</sub>(111) and tetragonal *t*-ZrO<sub>2</sub>(101) surface systems, respectively. The *m*-ZrO<sub>2</sub>(111) and *t*-ZrO<sub>2</sub>(101) surface systems were chosen because they are the thermodynamically most stable ones [52]; in other words, the surfaces have the smallest surface energy and were thus the most abundant forms in nature. The vacuum space is larger than 10.2 Å for both systems. *m*-ZrO<sub>2</sub>(111)-(1 × 1) and *t*-ZrO<sub>2</sub>(101)-(2 × 1) surfaces consisted of 9 layers (three Zr and six O layers) in which the 6 bottom layers were fixed at the equilibrium lattice constants and the other layers were fully relaxed. Based on the surface systems, a single Pd atom was adsorbed at the top surfaces, and one O atom was placed at the top of the Pd/ZrO<sub>2</sub> surfaces. Brillouin zone integrations for Pd/ZrO<sub>2</sub> was conducted using 6 × 6 × 1 Monkhorst-Pack grids [53], with the first-order Methfessel-Paxton smearing [54] with a width of 0.1 eV. The surface systems were optimized until the total energy change upon two steps of the electronic self-consistent loop less than 10<sup>-4</sup> eV.

The oxygen desorption energy ( $E_{\text{des}}$ , i.e., an energy required to detach O atom from O-Pd/ZrO<sub>2</sub>) of the O-Pd/ZrO<sub>2</sub> surface systems was calculated as follows.

$$E_{\text{des}} = E_{\text{Pd}} - E_{\text{Pd-O}} + E_{\text{O}} \quad (6)$$

where  $E_{\text{Pd}}$  is the total energy of the surface system containing one Pd,  $E_{\text{Pd-O}}$  is the total energy of surface systems with O-Pd, and  $E_{\text{O}}$  is the total energy of 1/2 O<sub>2</sub>.

**Table 2**

Specific surface areas (S<sub>BET</sub>), total pore volumes (V<sub>P</sub>), and average pore sizes (D<sub>P</sub>) of the ZrO<sub>2</sub>(x) supports and Pd/ZrO<sub>2</sub>(x) catalysts determined from the N<sub>2</sub>-sorption isotherms.

Digestion temperature (°C)	ZrO <sub>2</sub>			Pd/ZrO <sub>2</sub>		
	S <sub>BET</sub> (m <sup>2</sup> /g)	V <sub>P</sub> <sup>a</sup> (cm <sup>3</sup> /g)	D <sub>P</sub> <sup>b</sup> (nm)	S <sub>BET</sub> (m <sup>2</sup> /g)	V <sub>P</sub> <sup>a</sup> (cm <sup>3</sup> /g)	D <sub>P</sub> <sup>b</sup> (nm)
30	17	0.093	15.0	15	0.091	19.2
50	33	0.131	12.8	29	0.127	14.7
70	71	0.217	10.6	68	0.205	10.6
85	123	0.341	10.5	111	0.331	11.6
100	157	0.386	9.5	148	0.389	10.2

<sup>a</sup> Obtained from the volume of N<sub>2</sub> adsorbed at P/P<sub>0</sub> = 0.995.

<sup>b</sup> Calculated from the desorption branch of the N<sub>2</sub> isotherm using the Barrett-Joyner-Halenda method.

## 3. Results and discussion

### 3.1. Effects of digestion temperature

#### 3.1.1. Physico-chemical properties of ZrO<sub>2</sub> supports and Pd/ZrO<sub>2</sub> catalysts

Following the successful preparation of the desired supported catalysts, we initially investigated the effect of digestion temperature on the characteristics of ZrO<sub>2</sub> supports and Pd/ZrO<sub>2</sub> catalysts. Fig. S2 shows the N<sub>2</sub>-sorption isotherms of the supports and catalysts prepared at digestion temperatures ranging from 30 to 100 °C. According to IUPAC classification, all isotherms could be categorized as type IV isotherms with type H2 hysteresis loops, indicating that all supports and catalysts exhibited mesoporous structures. From the isotherms, the BET surface areas, total pore volumes, and average pore sizes are summarized in Table 2. As shown in Table 2, the BET surface areas of the ZrO<sub>2</sub>(x) supports increased upon increasing the digestion temperature [33,36,38]. This is because dissolution and recrystallization occur during the digestion process, and higher digestion temperatures promoted this phenomenon resulting in the developments of small homogeneous ZrO<sub>2</sub> particles. The HR-TEM images in Fig. S3 clearly show this tendency depending on digestion temperature. Of the various samples examined, ZrO<sub>2</sub>(100) exhibited the highest BET surface area (157 m<sup>2</sup>/g), which was a higher value than that previously reported for a ZrO<sub>2</sub> support [1,22,23,55,56]. In addition, the BET surface areas of the Pd catalysts decreased slightly following the impregnation due to partial pore blockage by the impregnated Pd species.

It is well known that pure ZrO<sub>2</sub> can exist as monoclinic (*m*)-, tetragonal (*t*)-, and cubic (*c*)-crystalline structures at atmospheric pressure [34,57,58]. Typically, the ZrO<sub>2</sub> prepared via a chemical precipitation method exhibited the monoclinic or the mixture of monoclinic and tetragonal crystalline forms with relatively low BET surface area (< 50 m<sup>2</sup>/g, [13,22,23]). This is because the *m*-ZrO<sub>2</sub> is the most thermodynamically stable polymorph at room temperature [39,58]. In our previous study [33], we reported that the crystalline structure of calcined ZrO<sub>2</sub> was largely influenced by the digestion temperature due to size effect, and *t*-ZrO<sub>2</sub> polymorph having relatively high BET surface area can be stabilized due to the lower surface energy of small crystallites [59–61]. As shown in Fig. 1A, the ZrO<sub>2</sub> samples digested at low temperatures (i.e., < 70 °C) contained both tetragonal (JCPDS No. 50-1089) and monoclinic (JCPDS No. 37-1484) phases, and the portion of tetragonal crystallites gradually increased as the digestion temperature approached 70 °C. Finally, ZrO<sub>2</sub> showed only a tetragonal structure above this temperature, due to the size effect [59–61].

Fig. 1B shows the XRD patterns of Pd/ZrO<sub>2</sub>(x) catalysts, and the relative proportions of the tetragonal and monoclinic phases following Pd impregnation are summarized in Table 3. As indicated, a reduction in the portion of the tetragonal phase was observed following impregnation for the Pd/ZrO<sub>2</sub>(30), Pd/ZrO<sub>2</sub>(50), and Pd/ZrO<sub>2</sub>(70) catalysts,

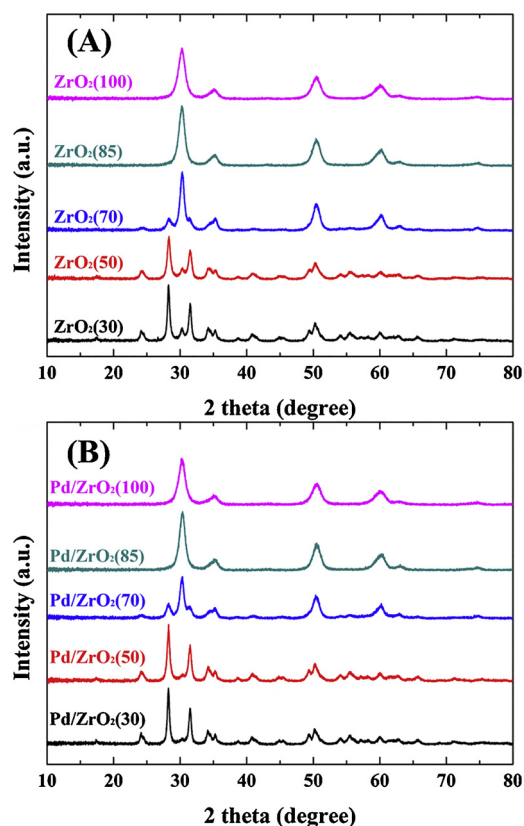


**Fig. 1.** XRD patterns of (A) the  $\text{ZrO}_2$ (x) supports, and (B) the  $\text{Pd}/\text{ZrO}_2$ (x) catalysts prepared at a range of digestion temperatures.

while  $\text{Pd}/\text{ZrO}_2(85)$  and  $\text{Pd}/\text{ZrO}_2(100)$  maintained a pure tetragonal phase. In addition, the crystal size of the monoclinic phase increased in the  $\text{Pd}/\text{ZrO}_2(30)$ ,  $\text{Pd}/\text{ZrO}_2(50)$ , and  $\text{Pd}/\text{ZrO}_2(70)$  catalysts after Pd impregnation. This is likely due to the low temperature degradation of the tetragonal to the monoclinic phase in the presence of water. Guo [62–64] proposed a degradation mechanism for the transition from the tetragonal to the monoclinic phase at relatively low temperatures (i.e., 60–400 °C), where this transformation is initiated by chemisorbed water molecules on oxygen vacancies of the  $\text{ZrO}_2$  lattice. In our case, Pd was impregnated on the support surface via an incipient wetness method with aqueous  $\text{Pd}(\text{NO}_3)_2$  solution. The XRD results outlined in Fig. 1B therefore indicated that tetragonal crystallites of  $\text{ZrO}_2$  can be transformed to the monoclinic phase during the impregnation procedure employed herein.

**Table 3**

Physicochemical properties of the  $\text{ZrO}_2$ (x) supports and  $\text{Pd}/\text{ZrO}_2$ (x) catalysts as determined by XRD and CO chemisorption measurements.

Digestion temperature (°C)	$\text{ZrO}_2$			$\text{Pd}/\text{ZrO}_2$			
	Crystal size <sup>a</sup> (nm)		Tetra. portion <sup>b</sup> (vol%)	Crystal size <sup>a</sup> (nm)		Tetra. portion <sup>b</sup> (vol%)	Pd dispersion <sup>c</sup> (%)
	Tetra. (2θ = 30.3°)	Mono. (2θ = 28.2°)		Tetra. (2θ = 30.3°)	Mono. (2θ = 28.2°)		
30	13.7	21.7	9.0	12.2	23.8	3.9	13.1
50	12.4	14.3	10.5	11.1	19.6	3.9	18.6
70	10.6	9.6	66.8	10.5	9.7	53	21.0
85	7.8	–	100	8.0	–	100	24.5
100	6.8	–	100	6.8	–	100	26.4

<sup>a</sup> The crystal sizes of the tetragonal and monoclinic  $\text{ZrO}_2$  phases were calculated using the Scherrer equation from the XRD peaks at  $2\theta = 30.3^\circ$  and  $28.2^\circ$ , respectively.

<sup>b</sup> The portion of the tetragonal phase was calculated by the empirical formulae outlined in the experimental section (i.e., Eqs. (2)–(4)).

<sup>c</sup> The dispersion and particle size of Pd were obtained from CO chemisorption measurements.

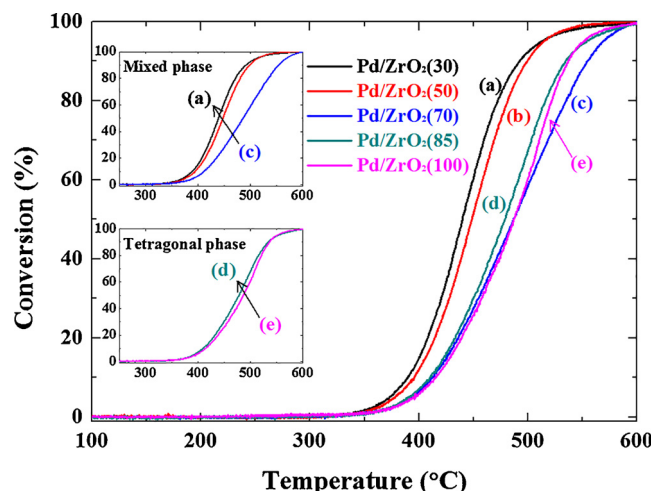


**Fig. 2.** Catalytic performances in the temperature-programmed methane combustion reaction (heating rate = 5 °C/min) over the  $\text{Pd}/\text{ZrO}_2$ (x) catalysts in the presence of 10 vol% water vapor as a function of reaction temperature: (a)  $\text{Pd}/\text{ZrO}_2(30)$ , (b)  $\text{Pd}/\text{ZrO}_2(50)$ , (c)  $\text{Pd}/\text{ZrO}_2(70)$ , (d)  $\text{Pd}/\text{ZrO}_2(85)$ , and (e)  $\text{Pd}/\text{ZrO}_2(100)$ .

### 3.1.2. Temperature-programmed reaction of methane combustion

Fig. 2 shows the results of the T.P. reactions of methane combustion over 1 wt%  $\text{Pd}/\text{ZrO}_2$ (x) catalysts in which the  $\text{ZrO}_2$  support was synthesized at different digestion temperatures. As indicated, the  $\text{Pd}/\text{ZrO}_2(30)$  and  $\text{Pd}/\text{ZrO}_2(50)$  catalysts, which exhibited relatively low BET surface areas, had low light-off temperatures (LOT) compared to the other samples. In this study, the LOT is defined as a temperature reached at 10% of  $\text{CH}_4$  conversion ( $T_{10}$ ), and these data including  $T_{50}$  and  $T_{90}$  are summarized in Table S1. However, this T.P. reaction is incomplete for testing the performance of the catalysts employed in this study, as it does not accurately represent the activation and deactivation processes (see Figs. 3 and 4 for a more detailed description). Thus, through these T.P. reactions, only a comparative study of the corresponding LOT was possible within the same crystalline phase of support. As shown in the insets of Fig. 2, in the same crystalline phase (i.e., in the mixed or tetragonal phase), the reaction was initiated at relatively low temperatures as the BET surface area of the support decreased.

### 3.1.3. Isothermal reaction of methane combustion

To investigate the catalytic performance including the activation and deactivation processes at a constant temperature, the isothermal reaction was carried out for 12 h, as shown in Fig. 3. Fig. 3A shows the results of the isothermal reactions at 500 °C, where it is apparent that

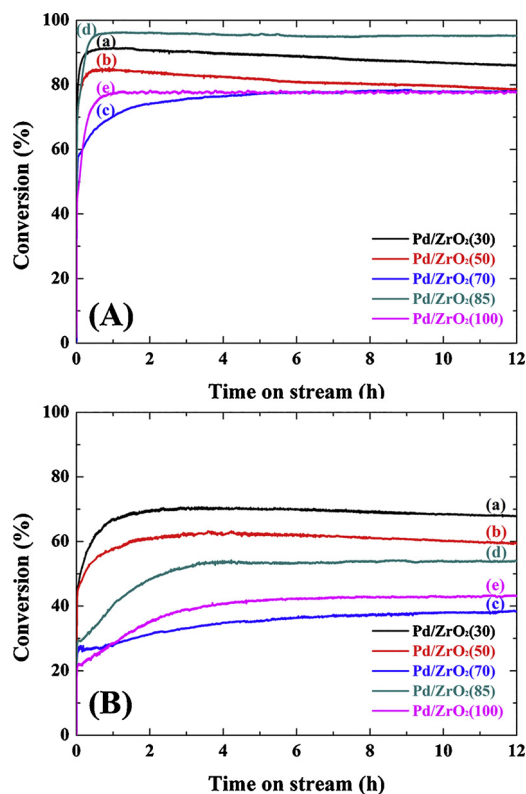


**Fig. 3.** Variation in the catalytic performances of the Pd/ZrO<sub>2</sub>(x) catalysts in the methane combustion reaction with time on stream in the presence of 10 vol % water vapor at (A) 500 and (B) 450 °C: (a) Pd/ZrO<sub>2</sub>(30), (b) Pd/ZrO<sub>2</sub>(50), (c) Pd/ZrO<sub>2</sub>(70), (d) Pd/ZrO<sub>2</sub>(85), and (e) Pd/ZrO<sub>2</sub>(100).

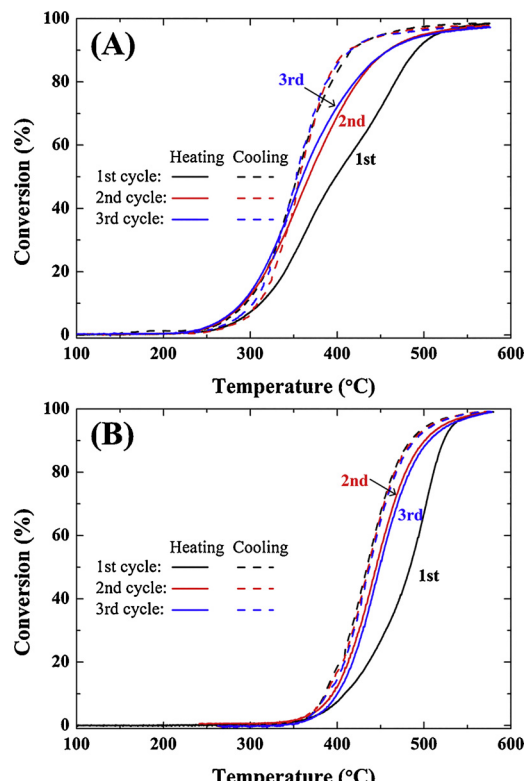


**Fig. 4.** Results of the cyclic temperature-programmed reactions over the Pd/ZrO<sub>2</sub>(85) catalyst in (A) the absence and (B) the presence of 10 vol% water vapor.

the conversion of methane over the Pd/ZrO<sub>2</sub>(x) catalysts decreased in following order: Pd/ZrO<sub>2</sub>(85) > Pd/ZrO<sub>2</sub>(30) > Pd/ZrO<sub>2</sub>(50) > Pd/ZrO<sub>2</sub>(100) > Pd/ZrO<sub>2</sub>(70). Although this tendency did not seem to correlate with the BET surface areas of the ZrO<sub>2</sub> supports, it was strongly related to the BET surface area in each crystalline structure. For example, in catalysts with mixed crystalline phases (i.e., Pd/ZrO<sub>2</sub>(30), Pd/ZrO<sub>2</sub>(50), and Pd/ZrO<sub>2</sub>(70)), the conversion was inversely proportional to the BET surface area. In addition, the conversion also increased as the BET surface area decreased in the Pd/ZrO<sub>2</sub>(85) and Pd/ZrO<sub>2</sub>(100) catalysts, which were supported on *t*-ZrO<sub>2</sub>. Although the reactivity order changed at 450 °C (see Fig. 3B, Pd/ZrO<sub>2</sub>(30) > Pd/ZrO<sub>2</sub>(50) > Pd/ZrO<sub>2</sub>(85) > Pd/ZrO<sub>2</sub>(100) > Pd/ZrO<sub>2</sub>(70)), the trend according to BET surface areas in same crystalline phases was consistent at both temperatures (i.e., Pd/ZrO<sub>2</sub>(30) > Pd/ZrO<sub>2</sub>(50) > Pd/ZrO<sub>2</sub>(70) in mixed phase, and Pd/ZrO<sub>2</sub>(85) > Pd/ZrO<sub>2</sub>(100) in tetragonal phase). It was expected that this variation in reactivity depending on reaction temperature was likely due to the effect of PdO particle sizes (see Table 3). More specifically, for the Pd species impregnated on ZrO<sub>2</sub> with a low BET surface area, relatively large particles were formed, thereby resulting in lower LOT, as indicated in Fig. 2 [65]. As such, these species reacted more effectively at lower temperatures, and this trend could be reversed at higher temperatures.

The digestion temperature during the preparation of support largely influences on catalytic activity as stated above, but also strongly affects the hydrothermal stability during the reaction, as summarized in Table 4. More specifically, the hydrothermal stabilities of the catalysts supported on pure *t*-ZrO<sub>2</sub> were superior to those of the catalysts supported on mixed phase ZrO<sub>2</sub>, with the exception of Pd/ZrO<sub>2</sub>(70). Although the Pd/ZrO<sub>2</sub>(70) catalyst did not experience significant deactivation, its activity was the lowest amongst the samples examined. As a result, the Pd/ZrO<sub>2</sub>(85) catalyst, which had the lowest BET surface area in the pure tetragonal structure, exhibited the best catalytic performance considering its activity and hydrothermal stability. In addition, the Pd/ZrO<sub>2</sub>(30) and Pd/ZrO<sub>2</sub>(50) catalysts underwent more severe deactivation at 450 °C than at 500 °C, and the remainder of the samples exhibited larger positive values of their deactivation rates ( $R_d$ ) at 450 °C, indicating that activation occurred throughout the reaction. This is likely due to the slower activation at lower temperatures.

### 3.1.4. Cyclic temperature-programmed reaction

From the isothermal reactions, all samples exhibited an initial activation period at both 450 and 500 °C. Although it was initially thought that this may be caused by an exothermic reaction, the temperature of the reactor was completely maintained within 1 °C of the set temperature throughout the reaction. In addition, this result also did not originate from an adsorption/desorption equilibrium, as the activation stage proceeded for a relatively long period of time (i.e., ~1 h).

**Table 4**

Conversion and deactivation rates during the isothermal reaction over the prepared Pd/ZrO<sub>2</sub>(x) catalysts.

Sample	Isothermal at 500 °C			Isothermal at 450 °C		
	X <sub>ini</sub> <sup>a</sup> (%)	X <sub>12 h</sub> <sup>b</sup> (%)	R <sub>d</sub> <sup>c</sup> (%/h)	X <sub>ini</sub> <sup>a</sup> (%)	X <sub>12 h</sub> <sup>b</sup> (%)	R <sub>d</sub> <sup>c</sup> (%/h)
Pd/ZrO <sub>2</sub> (30)	91.2	86.2	-0.46	72.1	67.8	-0.50
Pd/ZrO <sub>2</sub> (50)	82.3	78.5	-0.38	64.6	59.1	-0.71
Pd/ZrO <sub>2</sub> (70)	77.8	78.1	0.03	34.5	38.4	0.94
Pd/ZrO <sub>2</sub> (85)	95.1	95.2	0.01	53.6	54.0	0.06
Pd/ZrO <sub>2</sub> (100)	77.6	77.6	0.00	42.2	43.0	0.16

<sup>a</sup> X<sub>ini</sub> indicates the initial conversion obtained by extrapolation to conversion at 0 h.

<sup>b</sup> X<sub>12 h</sub> is the conversion after 12 h on stream.

<sup>c</sup> The deactivation rate (R<sub>d</sub>) was calculated using the following expression: R<sub>d</sub> = -(X<sub>ini</sub> - X<sub>12 h</sub>)/(X<sub>ini</sub> · 12 h) × 100.

Interestingly, Demoulin et al. [17] also reported activation in the methane combustion reaction over Pd/Al<sub>2</sub>O<sub>3</sub> catalysts, and they proposed that this was caused by the formation of highly oxidized Pd species or reconstruction (surface roughening) of the active sites. To further analyze this activation phenomenon in our Pd/ZrO<sub>2</sub> system, cyclic T.P. reactions were carried out over the Pd/ZrO<sub>2</sub>(85) catalyst under dry (Fig. 4A) and wet (Fig. 4B) conditions. As indicated, the conversions achieved during the second heating process were higher than those of first heating process under both conditions, and were comparable to those of the third cycle. It was therefore demonstrated that in the system examined herein, activation took place over the Pd/ZrO<sub>2</sub>(x) catalysts under both dry and wet conditions.

### 3.1.5. XPS study

In addition to the particle size, the oxidation state of the supported Pd species also influences on the catalytic performance in the methane combustion reaction. Although Pd can be present in the form of Pd°, Pd<sup>2+</sup>, or Pd<sup>4+</sup>, the Pd species originating from PdO or PdO<sub>x</sub> is generally accepted as the active species for the combustion reaction [14,22,66–69]. Although the XPS analysis is considered as one of the most powerful tools for determining the oxidation states of catalysts, it was difficult to quantitatively analyze due to spectral overlap of Pd 3d<sub>5/2</sub> and Zr 3p<sub>3/2</sub> spectra [22], as shown in Fig. S4. To address this issue, deconvolution was performed according to the following criteria, and the results are summarized in Table S2. Firstly, since it was confirmed that the BET surface areas of the ZrO<sub>2</sub>(x) supports increased as a function of digestion temperature, the XPS intensity of the observed Pd species per unit area gradually decreased as the digestion temperature was increased. This is because the outer surface concentration is directly proportional to its peak intensity [70]. Secondly, in our previous work [33], it was confirmed that the formation of hydroxyl groups progressively developed on the ZrO<sub>2</sub> surface upon increasing the digestion temperature, and thus deconvolution was carried out to increase the intensity of the Zr(OH)<sub>x</sub> peak as a function of digestion temperature.

Fig. 5 indicates the Pd<sup>2+</sup>/Pd° atomic ratios in the Pd 3d<sub>5/2</sub> spectra of the Pd/ZrO<sub>2</sub>(x) catalysts, and when plotted as a function of digestion temperature, a volcano-shaped curve was obtained. In addition, the Pd<sup>2+</sup>/Pd° ratios in the pure t-ZrO<sub>2</sub> supported catalysts were higher than those in the mixed phase supported catalysts. Furthermore, as indicated in Table 4, the Pd/ZrO<sub>2</sub>(70), Pd/ZrO<sub>2</sub>(85), and Pd/ZrO<sub>2</sub>(100) catalysts exhibited excellent hydrothermal stabilities at both 450 and 500 °C for 12 h. Interestingly, as shown in Fig. 5, the Pd<sup>2+</sup>/Pd° ratios in these samples were either maintained or slightly increased during the reaction at 500 °C in the presence of 10 vol% water vapor, due to the activation process. In contrast, the Pd<sup>2+</sup>/Pd° ratios of the Pd/ZrO<sub>2</sub>(30) and Pd/ZrO<sub>2</sub>(50) catalysts decreased following the reaction, likely due to

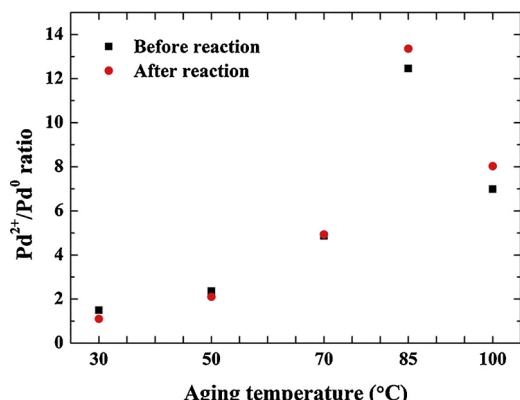


Fig. 5. Pd<sup>2+</sup>/Pd° ratios of the Pd/ZrO<sub>2</sub>(x) catalysts before and after the reaction at 500 °C for 12 h in the presence of 10 vol% water vapor obtained from Pd 3d<sub>5/2</sub> and Zr 3p<sub>3/2</sub> XPS spectra.

catalyst deactivation. Moreover, a change in the crystalline phase of ZrO<sub>2</sub> was not detected in the XRD patterns of spent catalysts as shown in Fig. S5, and thus these results demonstrated that the activation and deactivation phenomena observed during the reaction were mainly caused by changes in the oxidation states of the supported Pd species [1,14,21].

### 3.2. Effects of digestion time and calcination temperature

#### 3.2.1. Characteristics of the remainder samples

In the previous chapter for the effects of digestion temperature, it was confirmed that t-ZrO<sub>2</sub> supported catalysts exhibited improved hydrothermal stabilities compared to the mixed phase ZrO<sub>2</sub> supported catalysts. Although conversion and stability varied with the digestion temperature, both the crystalline phase and the BET surface area of the support were concurrently influenced by the digestion temperature. Therefore, to clearly confirm the effects of varying BET surface areas of supports on the catalytic performance, additional experiments were conducted using the prepared ZrO<sub>2</sub>(A) and ZrO<sub>2</sub>(B) supports, in addition to the commercially obtained ZrO<sub>2</sub>(C) support.

As discussed in the experimental section, the ZrO<sub>2</sub>(A) and ZrO<sub>2</sub>(B) supports were synthesized according to the procedure employed for the ZrO<sub>2</sub>(100) support, but using an extended digestion time of 240 h and different calcination temperatures (i.e., 700 °C for ZrO<sub>2</sub>(A) and 600 °C for ZrO<sub>2</sub>(B)). The BET surface areas of these supports were found to be higher than those of the ZrO<sub>2</sub>(100) support due to longer digestion time [33,36–39]. As outlined in Table 5, the BET surface areas of these supports increased in the following order: ZrO<sub>2</sub>(85) < ZrO<sub>2</sub>(100) < ZrO<sub>2</sub>(A) < ZrO<sub>2</sub>(B). In addition, as indicated in Fig. S6A, the ZrO<sub>2</sub>(85), ZrO<sub>2</sub>(100), ZrO<sub>2</sub>(A), and ZrO<sub>2</sub>(B) samples exhibited pure tetragonal crystalline structures, and no changes in the crystalline phase were observed following Pd impregnation (Fig. S6B). In contrast, ZrO<sub>2</sub>(C) contained pure monoclinic crystallites.

#### 3.2.2. Isothermal reaction of methane combustion

Fig. 6 shows the results of the isothermal reactions at 450 °C in the presence of 10 vol% water vapor. With the exception of Pd/ZrO<sub>2</sub>(C), the initial activation phenomenon was observed for all samples, and no significant deactivation was observed, thereby indicating that the t-ZrO<sub>2</sub> supported catalysts exhibited excellent hydrothermal stabilities. Moreover, the conversion trend was inversely proportional to the BET surface areas of the supports, likely due to the influence of PdO particle size [17,65,71]. From the CO chemisorption measurements, the dispersions and particle sizes of the supported Pd species were obtained, and the results are summarized in Table 5. It was confirmed that the

Table 5

Physicochemical properties of the additional ZrO<sub>2</sub> supports and Pd/ZrO<sub>2</sub> catalysts determined by N<sub>2</sub>-sorption and CO chemisorption measurements.

Sample	ZrO <sub>2</sub>		Pd/ZrO <sub>2</sub>		
	S <sub>BET</sub> (m <sup>2</sup> /g)	V <sub>p</sub> <sup>a</sup> (cm <sup>3</sup> /g)	D <sub>p</sub> <sup>b</sup> (nm)	Pd dispersion <sup>c</sup> (%)	Pd particle size <sup>c</sup> (nm)
ZrO <sub>2</sub> (85)	123	0.341	10.5	24.5	4.6
ZrO <sub>2</sub> (100)	157	0.386	9.5	26.4	4.2
ZrO <sub>2</sub> (A)	178	0.475	10.3	26.5	4.2
ZrO <sub>2</sub> (B)	219	0.555	9.9	27.2	4.1
ZrO <sub>2</sub> (C)	103	0.313	9.4	43.4	2.6

<sup>a</sup> Obtained from the volume of N<sub>2</sub> adsorbed at P/P<sub>0</sub> = 0.995 in the N<sub>2</sub>-sorption isotherm.

<sup>b</sup> Calculated from the desorption branch of the N<sub>2</sub> isotherm using the Barrett-Joyner-Halenda method.

<sup>c</sup> The dispersion and particle size of Pd were obtained from CO chemisorption measurement.

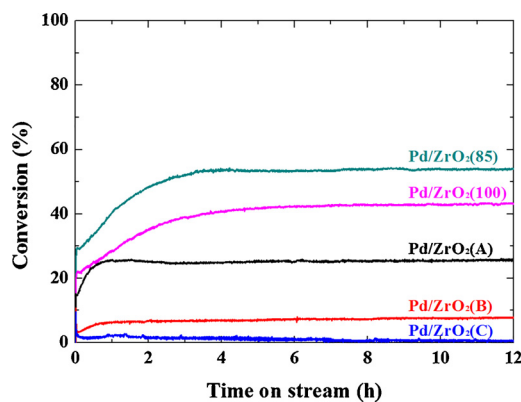


**Fig. 6.** Catalytic performance of the Pd/ZrO<sub>2</sub> catalysts in the methane combustion reaction at 450 °C for 12 h in the presence of 10 vol% water vapor.

dispersion of Pd on the support surface gradually increased from 24.50 to 27.22% as the BET surface area increased, indicating that smaller particles were formed on ZrO<sub>2</sub> having relatively high BET surface areas. It could therefore be concluded that smaller BET surface areas resulted in higher catalytic activities in the case of the *t*-ZrO<sub>2</sub> supported catalysts. In contrast, the *m*-ZrO<sub>2</sub> supported catalyst, Pd/ZrO<sub>2</sub>(C), exhibited the highest dispersion and the smallest particle size despite its relatively low BET surface area [13]. This is because the difference in metal-support interactions between *m*-ZrO<sub>2</sub> and *t*-ZrO<sub>2</sub> catalysts, and this effect will be further discussed in DFT calculation section. Consequently, the Pd/ZrO<sub>2</sub>(C) catalyst exhibited a negligible activity at 450 °C in the presence of 10 vol% water vapor, due to the smallest PdO particle size. In addition, the catalytic activity can be also expressed in terms of turnover frequency (TOF), which was quantified based on the number of active site as shown in Fig. S7. Since the catalysts employed herein exhibited the higher activity with increasing particles size of impregnated Pd, the TOF data had same trend with that of CH<sub>4</sub> conversion.

### 3.2.3. Reducibility test by CH<sub>4</sub>-TPR

The reducibility of impregnated PdO species has also attracted great interest in the context of the methane combustion reaction, as this reaction is known to follow the Mars and van Krevelen reduction-oxidation pathway [11,24,43,65,69]. In this mechanism, the first step involves the reduction of PdO by methane, followed by the re-oxidation of Pd by oxygen present in the feed stream or by lattice oxygen. Thus, the reduction temperatures indicated in the TPR profiles may correlate with the observed catalytic performances [3,19,24,72,73]. In this context, CH<sub>4</sub>-TPR profiles of the Pd/ZrO<sub>2</sub> catalysts shown in Fig. 7 indicated that the reduction temperatures gradually shifted towards

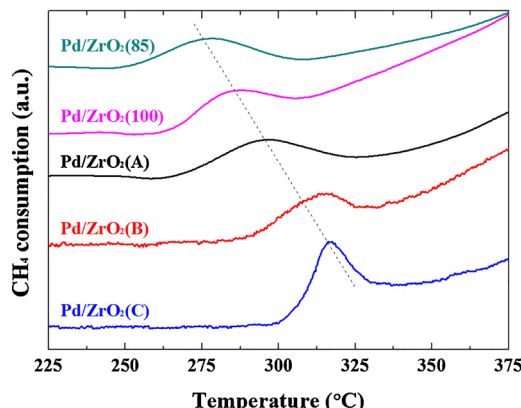


**Fig. 7.** Reduction behaviors of the Pd/ZrO<sub>2</sub> catalysts as determined by CH<sub>4</sub>-TPR.

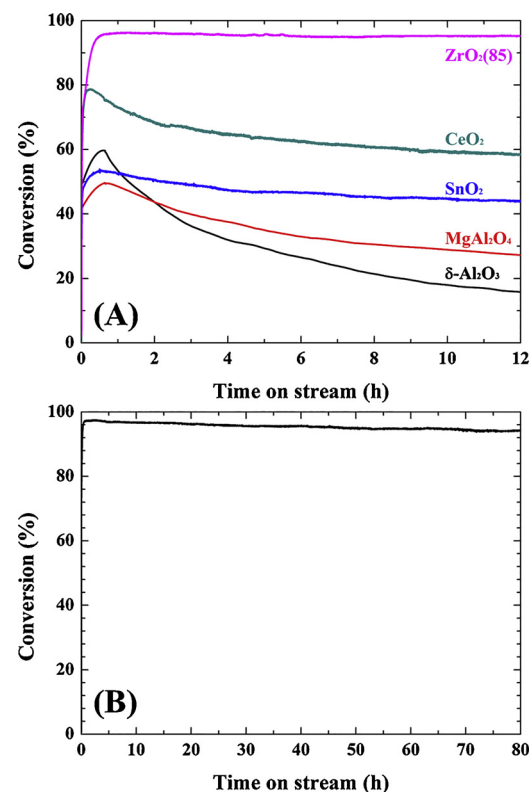


**Fig. 8.** (A) Comparison of the activities and hydrothermal stabilities of the various 1 wt% Pd catalysts in the methane combustion reaction, and (B) long-term stability of the Pd/ZrO<sub>2</sub>(85) catalyst for 80 h. All reactions were carried out at 500 °C in the presence of 10 vol% water vapor.

lower temperatures as particle size of the Pd species increased (see Table 5). More specifically, the Pd/ZrO<sub>2</sub>(85) catalyst exhibited the lowest reduction temperature, thereby indicating that the PdO species in this catalyst was more readily reduced than those of the other samples. These results therefore suggest that the excellent catalytic performance of Pd/ZrO<sub>2</sub>(85) can be attributed to the high reducibility of the PdO species, and is influenced by the effect of the PdO particle size.

### 3.2.4. Comparative study with various catalysts

To further confirm the efficiency of the Pd/ZrO<sub>2</sub>(85) catalyst, we synthesized a number of supports that are widely employed in the field of methane combustion, including Al<sub>2</sub>O<sub>3</sub>, MgAl<sub>2</sub>O<sub>4</sub>, SnO<sub>2</sub>, and CeO<sub>2</sub> (see Fig. S8 and Table S3 for detailed characteristics of the supports). Fig. 8A shows the results of isothermal reactions over supported Pd catalysts at 500 °C in the presence of 10 vol% water vapor, where it is apparent that the Pd/ZrO<sub>2</sub>(85) catalyst exhibited the best catalytic performance amongst all catalysts examined. In addition, no significant deactivation (deactivation rate = -0.27%/h) was observed for 80 h under the experimental conditions employed, as shown in Fig. 8B.

### 3.3. A DFT study for calculating the oxygen desorption energy

In our previous chapter, it was confirmed that the size of impregnated Pd species supported on *t*-ZrO<sub>2</sub> is inversely proportional to the BET surface area of support. In addition, the reducibility was strongly related to the particles size of Pd species, thereby varying the catalytic performance. However, a direct comparison between *m*- and *t*-ZrO<sub>2</sub> supported PdO catalysts was not possible. This is because *m*-ZrO<sub>2</sub> supported catalyst exhibited the highest metal dispersion, even though the BET surface area was relatively low (see Table 5). Therefore, the DFT calculations were performed to compare the *m*- and *t*-ZrO<sub>2</sub> supported catalysts under theoretically equal conditions, as follows.

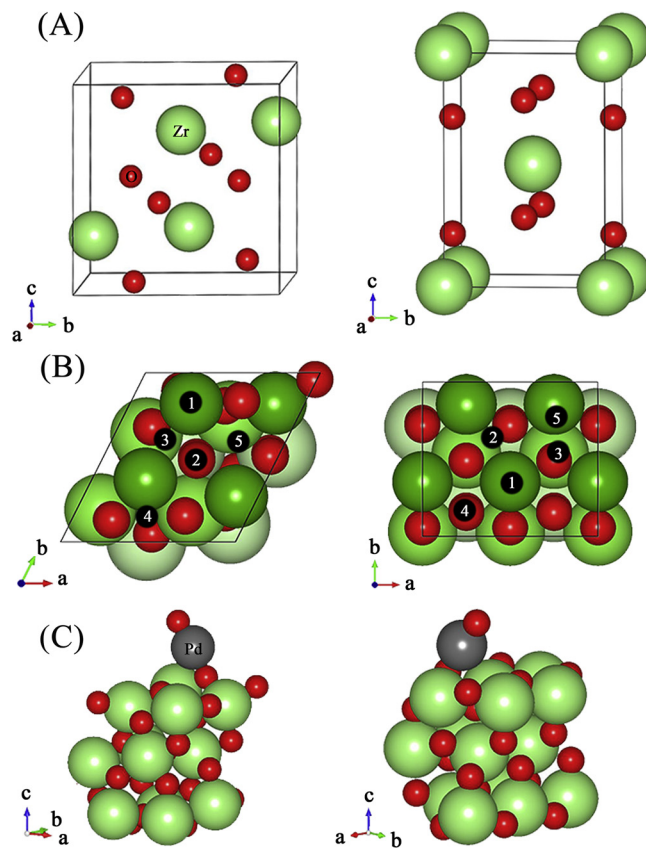


**Fig. 9.** (A) Bulk structures of *m*-ZrO<sub>2</sub> (left) and *t*-ZrO<sub>2</sub> (right). (B) Top views of *m*-ZrO<sub>2</sub>(1 × 1) and *t*-ZrO<sub>2</sub>(2 × 1) surfaces. (C) Side views of O-Pd adsorbed on *m*-ZrO<sub>2</sub>(1 × 1) and *t*-ZrO<sub>2</sub>(2 × 1). The black dots (1–5) indicate the adsorption sites of Pd-O. Large green, small red, large gray spheres represent Zr, O, and Pd, respectively (For interpretation of the references to colour in this figure legend, the reader is referred to the web version of this article).

### 3.3.1. Bulk and surface structures of ZrO<sub>2</sub>

The bulk structures of *m*-ZrO<sub>2</sub> and *t*-ZrO<sub>2</sub> were optimized as shown in Fig. 9A. The equilibrium lattice constants of *m*-ZrO<sub>2</sub> and *t*-ZrO<sub>2</sub> were *a* = 5.27, *b* = 5.31, and *c* = 5.40 Å for *m*-ZrO<sub>2</sub>, and *a* = *b* = 3.63 and *c* = 5.26 Å for *t*-ZrO<sub>2</sub>, which shows good agreement with those of previous experimental study [74] (*a* = 5.19, *b* = 5.25, and *c* = 5.35 Å for *m*-ZrO<sub>2</sub>, and *a* = *b* = 3.61 and *c* = 5.25 Å for *t*-ZrO<sub>2</sub>). Based on the bulk structures, *m*-ZrO<sub>2</sub>(111)-(1 × 1) and *t*-ZrO<sub>2</sub>(101)-(2 × 1) surfaces (Fig. 9B), which are the most stable surfaces in nature (i.e., the surfaces are the most abundant forms) [52], were used to construct O-Pd/ZrO<sub>2</sub> systems (Fig. 9C) and calculate the desorption energy (*E*<sub>des</sub>) of single oxygen atom from O-Pd/ZrO<sub>2</sub>.

### 3.3.2. Oxygen desorption energy from O-Pd/ZrO<sub>2</sub>

Pd and O atoms were adsorbed on the adsorption sites of both ZrO<sub>2</sub> surfaces (Fig. 9B), and *E*<sub>des</sub> was calculated by removing O atom from O-Pd/ZrO<sub>2</sub> systems. The largest *E*<sub>des</sub> were 1.03 and 0.85 eV for *m*-ZrO<sub>2</sub> and *t*-ZrO<sub>2</sub>, respectively, implying that oxygen removal is more difficult from the *m*-ZrO<sub>2</sub> surface than the *t*-ZrO<sub>2</sub> surface. Details of the *E*<sub>des</sub> calculation data are shown in Tables S4 and S5. As shown in Table 5, although the BET surface area of *m*-ZrO<sub>2</sub> support was relatively low, the highest metal dispersion was exhibited. Thus, the variations in reducibility shown in Fig. 7 would be mainly caused by the difference in particle size, rather than crystalline phase. However, the results obtained from the DFT calculations clearly demonstrate that *t*-ZrO<sub>2</sub> supported PdO catalyst was more reducible than *m*-ZrO<sub>2</sub> supported catalyst under the theoretically equal conditions. Therefore, this result shows that *t*-ZrO<sub>2</sub> is more advantageous than *m*-ZrO<sub>2</sub> as a support for catalytic

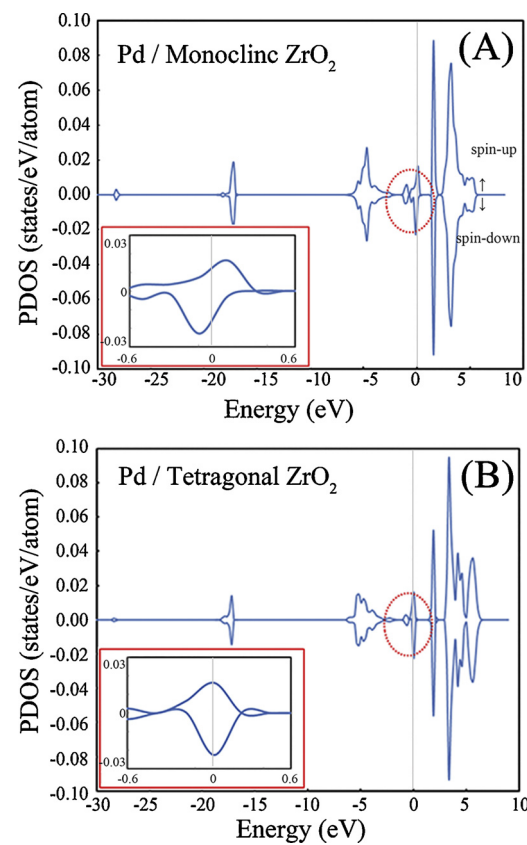


**Fig. 10.** PDOS of the 3d orbitals of Pd on A) *m*-ZrO<sub>2</sub>(111) and B) *t*-ZrO<sub>2</sub>(101), respectively. Insets represent a closer range (from −0.6 to 0.6 eV) near the Fermi level. The Fermi energy is referenced at 0 eV.

methane combustion, in terms of reducibility of impregnated Pd species.

### 3.3.3. Electronic properties of Pd/ZrO<sub>2</sub>

Projected density of states (PDOS) analysis was conducted to understand the fundamental mechanism for the larger *E*<sub>des</sub> of *m*-ZrO<sub>2</sub> than that of *t*-ZrO<sub>2</sub>. The oxygen desorption energy from O-Pd/ZrO<sub>2</sub> is significantly influenced by the electronic property of Pd that is affected by the types of the ZrO<sub>2</sub> surfaces. The PDOS of 3d orbitals of Pd was thus analyzed. As shown in Fig. 10, the electron density of Pd/*m*-ZrO<sub>2</sub> near the Fermi level is higher than that of Pd/*t*-ZrO<sub>2</sub> (see the insets of each Figure). To quantitatively compare, the areas of PDOS (i.e., the product of *x* and *y* axes) of both systems were calculated depending on the range of energy level from −0.6 to 0 eV, resulting in 0.008 and 0.004 states/atom for *m*-ZrO<sub>2</sub> and *t*-ZrO<sub>2</sub>, respectively. The higher electron density, or the larger PDOS area, near the fermi level may be responsible for the stronger interaction of O atom with Pd/*m*-ZrO<sub>2</sub>, resulting from the larger *E*<sub>des</sub> as pointed out by Hyman and Medlin [75]. Furthermore, the higher electron density of Pd/*m*-ZrO<sub>2</sub> was attributed to the higher electron density of O 2p orbital of *m*-ZrO<sub>2</sub> compared to that of *t*-ZrO<sub>2</sub>. More information of the PDOS analysis is shown in Table S6, Figs. S9 and S10.

## 4. Conclusions

We herein described the synthesis of Pd/ZrO<sub>2</sub> catalysts using different digestion temperatures, digestion times, and calcination temperatures, followed by their application in the catalytic methane combustion. Upon increasing the digestion temperature, the BET surface areas of the supports gradually increased, and their crystalline structures were transformed from mixed phase (monoclinic and tetragonal)

to pure tetragonal phase. From the results of isothermal reactions, it was apparent that the *t*-ZrO<sub>2</sub> supported catalysts exhibited superior hydrothermal stabilities than the mixed phase ZrO<sub>2</sub> supported catalysts. In addition, ZrO<sub>2</sub> supports were prepared having different digestion times and calcination temperatures to confirm the effect of the BET surface area in the tetragonal structure on catalytic activity. As a result, the Pd/ZrO<sub>2</sub>(85) catalyst, which had the smallest BET surface area of the various *t*-ZrO<sub>2</sub> supported catalysts employed herein, exhibited the optimal catalytic performance. It was expected that this is due to the formation of large PdO particles on ZrO<sub>2</sub> exhibiting relatively low BET surface areas. This is of particular importance as larger PdO particles were more readily reduced than smaller particles, as determined by CH<sub>4</sub>-TPR. From the DFT calculations, the oxygen desorption energies of *m*- and *t*-ZrO<sub>2</sub> supported PdO were theoretically measured, and it was revealed that PdO supported on *m*-ZrO<sub>2</sub> is harder to reduce than the PdO supported on *t*-ZrO<sub>2</sub>. This is because electron density of Pd/*m*-ZrO<sub>2</sub> near the Fermi level is higher than that of Pd/*t*-ZrO<sub>2</sub>.

## Acknowledgments

This research was supported by Basic Science Research Program through the National Research Foundation of Korea (NRF) funded by the Ministry of Science and ICT (2017R1A6A3A11027830).

## Appendix A. Supplementary data

Supplementary material related to this article can be found, in the online version, at doi:<https://doi.org/10.1016/j.apcatb.2018.03.101>.

## References

- [1] K. Narui, K. Furuta, H. Yata, A. Nishida, Y. Kohtoku, T. Matsuzaki, *Catal. Today* 45 (1998) 173–178.
- [2] Y. Liu, S. Wang, D. Gao, T. Sun, C. Zhang, S. Wang, *Fuel Process. Technol.* 111 (2013) 55–61.
- [3] L. Liotta, G. Di Carlo, G. Pantaleo, G. Deganello, *Catal. Commun.* 6 (2005) 329–336.
- [4] R. Hayes, *Chem. Eng. Sci.* 59 (2004) 4073–4080.
- [5] X. Pan, Y. Zhang, Z. Miao, X. Yang, *J. Energy Chem.* 22 (2013) 610–616.
- [6] Y. Liu, S. Wang, T. Sun, D. Gao, C. Zhang, S. Wang, *Appl. Catal. B: Environ.* 119 (2012) 321–328.
- [7] V.R. Choudhary, B.S. Upadhe, S.G. Pataskar, A. Keshavaraja, *Angew. Chem. Int. Ed.* 35 (1996) 2393–2395.
- [8] R. Anderson, K. Stein, J. Feenan, L. Hofer, *Ind. Eng. Chem.* 53 (1961) 809–812.
- [9] A.C. Gluhoi, B.E. Nieuwenhuys, *Catal. Today* 119 (2007) 305–310.
- [10] S. Ayabe, H. Omoto, T. Utaka, R. Kikuchi, K. Sasaki, Y. Teraoka, K. Eguchi, *Appl. Catal. A: Gen.* 241 (2003) 261–269.
- [11] D. Ciuparu, L. Pfefferle, *Catal. Today* 77 (2002) 167–179.
- [12] K. Persson, A. Ersson, K. Jansson, N. Iverlund, S. Järås, *J. Catal.* 231 (2005) 139–150.
- [13] S. Guerrero, P. Araya, E.E. Wolf, *Appl. Catal. A: Gen.* 298 (2006) 243–253.
- [14] A. Baylet, S. Royer, P. Marecot, J.-M. Tatibouet, D. Duprez, *Appl. Catal. B: Environ.* 77 (2008) 237–247.
- [15] D. Gao, C. Zhang, S. Wang, Z. Yuan, S. Wang, *Catal. Commun.* 9 (2008) 2583–2587.
- [16] G. Diannan, W. Sheng, C. ZHANG, Y. Zhongshan, W. Shudong, *Chin. J. Catal.* 29 (2008) 1221–1225.
- [17] O. Demoulin, G. Rupprechter, I. Seunier, B. Le Clef, M. Navez, P. Ruiz, *J. Phys. Chem. B* 109 (2005) 20454–20462.
- [18] W. Yang, D. Li, D. Xu, X. Wang, *J. Nat. Gas Chem.* 18 (2009) 458–466.
- [19] T. Takeguchi, S. Aoyama, J. Ueda, R. Kikuchi, K. Eguchi, *Top. Catal.* 23 (2003) 159–162.
- [20] T. Takeguchi, O. Takeoh, S. Aoyama, J. Ueda, R. Kikuchi, K. Eguchi, *Appl. Catal. A: Gen.* 252 (2003) 205–214.
- [21] F. Yin, S. Ji, P. Wu, F. Zhao, C. Li, *J. Catal.* 257 (2008) 108–116.
- [22] J.-H. Park, J.H. Cho, Y.J. Kim, E.S. Kim, H.S. Han, C.-H. Shin, *Appl. Catal. B: Environ.* 160–161 (2014) 135–143.
- [23] K. Nomura, K. Noro, Y. Nakamura, H. Yoshida, A. Satsuma, T. Hattori, *Catal. Lett.* 58 (1999) 127–130.
- [24] L.-f. Yang, C.-k. Shi, X.-e. He, J.-x. Cai, *Appl. Catal. B: Environ.* 38 (2002) 117–125.
- [25] M. Bhagiyalakshmi, R. Anuradha, S.-D. Park, T.-S. Park, W.-S. Cha, H.-T. Jang, *Bull. Korean Chem. Soc.* 31 (2010) 120–124.
- [26] N.M. Kinnunen, J.T. Hirvi, K. Kallinen, T. Maunula, M. Keenan, M. Suvanto, *Appl. Catal. B: Environ.* 207 (2017) 114–119.
- [27] M. Monai, T. Montini, M. Melchionna, T. Duchon, P. Kúš, C. Chen, N. Tsud, L. Nasi, K.C. Prince, K. Veltruská, *Appl. Catal. B: Environ.* 202 (2017) 72–83.
- [28] A.T. Gremminger, H.W.P. de Carvalho, R. Popescu, J.-D. Grunwaldt, O. Deutschmann, *O. Deutschmann, Catal. Today* 258 (2015) 470–480.
- [29] A. Gremminger, P. Lott, M. Merts, M. Casapu, J.-D. Grunwaldt, O. Deutschmann, *Appl. Catal. B: Environ.* 218 (2017) 833–843.
- [30] Z. Pu, H. Zhou, Y. Zheng, W. Huang, X. Li, *Appl. Surf. Sci.* 410 (2017) 14–21.
- [31] C. Cullis, T. Nevell, D. Trimm, *J. Chem. Soc.—Faraday Trans. 1* (68) (1972) 1406–1412.
- [32] R. Burch, F. Urbano, P. Loader, *Appl. Catal. A: Gen.* 123 (1995) 173–184.
- [33] E. Hong, S.W. Baek, M. Shin, Y.-W. Suh, C.-H. Shin, *J. Ind. Eng. Chem.* 54 (2017) 137–145.
- [34] A. Mondal, S. Ram, *J. Am. Ceram. Soc.* 87 (2004) 2187–2194.
- [35] A. Clearfield, *J. Mater. Res.* 5 (1990) 161–162.
- [36] G. Chuah, S. Jaenicke, S.A. Cheong, K. Chan, *Appl. Catal. A: Gen.* 145 (1996) 267–284.
- [37] G. Chuah, *Catal. Today* 49 (1999) 131–139.
- [38] G. Chuah, S. Jaenicke, *Appl. Catal. A: Gen.* 163 (1997) 261–273.
- [39] G. Chuah, S. Jaenicke, B. Pong, *J. Catal.* 175 (1998) 80–92.
- [40] W. Stichert, F. Schüth, *Chem. Mater.* 10 (1998) 2020–2026.
- [41] H.-I. Sim, J.-H. Park, J.H. Cho, J.-H. Ahn, M.-S. Choi, C.-H. Shin, *Korean Chem. Eng. Res.* 51 (2013) 208–213.
- [42] H.J. Lee, D.-C. Kang, S.H. Pyen, M. Shin, Y.-W. Suh, H. Han, C.-H. Shin, *Appl. Catal. A: Gen.* 531 (2017) 13–20.
- [43] X. Zou, Z. Rui, S. Song, H. Ji, *J. Catal.* 338 (2016) 192–201.
- [44] G. Kresse, J. Hafner, *Phys. Rev. B* 47 (1993) 558.
- [45] G. Kresse, J. Hafner, *Phys. Rev. B* 49 (1994) 14251.
- [46] G. Kresse, J. Furthmüller, *Phys. Rev. B* 54 (1996) 11169.
- [47] G. Kresse, J. Furthmüller, *Comput. Mater. Sci.* 6 (1996) 15–50.
- [48] P.E. Blöchl, *Phys. Rev. B* 50 (1994) 17953.
- [49] G. Kresse, D. Joubert, *Phys. Rev. B* 59 (1999) 1758.
- [50] J.P. Perdew, K. Burke, M. Ernzerhof, *Phys. Rev. Lett.* 77 (1996) 3865.
- [51] I. Takahashi, O. Koga, N. Hoshi, Y. Hori, *J. Electroanal. Chem.* 533 (2002) 135–143.
- [52] A. Hofmann, S.J. Clark, M. Oppel, I. Hahnorf, *Phys. Chem. Chem. Phys.* 4 (2002) 3500–3508.
- [53] H.J. Monkhorst, J.D. Pack, *Phys. Rev. B* 13 (1976) 5188.
- [54] M. Methfessel, A. Paxton, *Phys. Rev. B* 40 (1989) 3616.
- [55] W.-S. Dong, K.-W. Jun, H.-S. Roh, Z.-W. Liu, S.-E. Park, *Catal. Lett.* 78 (2002) 215–222.
- [56] P. Taghavinezhad, M. Haghghi, R. Alizadeh, *Korean J. Chem. Eng.* 34 (2017) 1346–1357.
- [57] S. Fabris, A.T. Paxton, M.W. Finnis, *Acta Mater.* 50 (2002) 5171–5178.
- [58] J.R. Kelly, I. Denry, *Dent. Mater.* 24 (2008) 289–298.
- [59] R. Garvie, M. Goss, *J. Mater. Sci.* 21 (1986) 1253–1257.
- [60] R. Garvie, *J. Phys. Chem.* 69 (1965) 1238–1243.
- [61] R. Garvie, *J. Phys. Chem.* 82 (1978) 218–224.
- [62] X. Guo, *J. Phys. Chem. Solids* 60 (1999) 539–546.
- [63] X. Guo, *Solid State Ionics* 112 (1998) 113–116.
- [64] X. Guo, *Chem. Mater.* 16 (2004) 3988–3994.
- [65] C.A. Müller, M. Maciejewski, R.A. Koepel, A. Baiker, *Catal. Today* 47 (1999) 245–252.
- [66] S. Yang, A. Maroto-Valiente, M. Benito-González, I. Rodriguez-Ramos, A. Guerrero-Ruiz, *Appl. Catal. B: Environ.* 28 (2000) 223–233.
- [67] Y.-H. Chin, M. García-Díéguez, E. Iglesia, *J. Phys. Chem. C* 120 (2016) 1446–1460.
- [68] Y. Lou, J. Ma, W. Hu, Q. Dai, L. Wang, W. Zhan, Y. Guo, X.-M. Cao, Y. Guo, P. Hu, *ACS Catal.* 6 (2016) 8127–8139.
- [69] K.-i. Fujimoto, F.H. Ribeiro, M. Avalos-Borja, E. Iglesia, *J. Catal.* 179 (1998) 431–442.
- [70] S.C. Fung, *J. Catal.* 58 (1979) 454–469.
- [71] P. Briot, M. Primet, *Appl. Catal.* 68 (1991) 301–314.
- [72] P. Castellazzi, G. Groppi, P. Forzatti, A. Baylet, P. Marécot, D. Duprez, *Catal. Today* 155 (2010) 18–26.
- [73] C.-k. Shi, L.-f. Yang, Z.-c. Wang, X.-e. He, J.-x. Cai, G. Li, X.-s. Wang, *Appl. Catal. A: Gen.* 243 (2003) 379–388.
- [74] R. Terki, G. Bertrand, H. Aourag, C. Coddet, *Mater. Sci. Semicond. Process.* 9 (2006) 1006–1013.
- [75] M.P. Hyman, J.W. Medlin, *J. Phys. Chem. C* 111 (2007) 17052–17060.